# Optimization of stripline-based microfluidic chips for high-resolution NMR

J. Bart [a], J.W.G. Janssen [b], P.J.M. van Bentum [b], A.P.M. Kentgens [b], J.G.E. Gardeniers [a,*]

[a] MESA+ Institute for Nanotechnology, University of Twente, P.O. Box 217, 7500 AE Enschede, The Netherlands
[b] Institute for Molecules and Materials, Radboud University Nijmegen, Toernooiveld 1, 6525 ED Nijmegen, The Netherlands

## ARTICLE INFO

## ABSTRACT

We here report on the optimization, fabrication and experimental characterization of a stripline-based microfluidic NMR probe, realized in a silicon substrate. The stripline geometry was modelled in respect of rf-homogeneity, sensitivity and spectral resolution. Using these models, optimal dimensional ratios were found, which hold for every sample size. Based on the optimized parameters, a simple integrated stripline-based microfluidic chip was realized. The fabrication of this chip is described in detail. We achieved a sensitivity of 0.47 nmol/$\sqrt{Hz}$ and a resolution of 0.7 Hz. The rf-homogeneity ($A_{810°}/A_{90°}$) was 76% and was proved to be suitable for 2D-NMR analysis of glucose.

© 2009 Elsevier Inc. All rights reserved.

## 1. Introduction

For reasons of efficiency, toxicity, waste reduction, sample control, performance, hyphenation conformity or simply limited availability, the ability to perform analytical operations on a small scale using so-called lab-on-a-chip devices is very appealing, and significant progress has been made in this field over the last decades [1,2]. Nuclear magnetic resonance (NMR) is one of the most powerful analysis methods in chemistry, biology and material sciences, providing local structural information and insight into molecular dynamics. The desire to apply NMR to very small sample volumes, as well as the need for more sensitive detection, has resulted in a thorough investigation of miniaturized detection coils [3–7]. The focus of this research has been mainly on the improvement in mass-sensitivity. For example, a more than two orders of magnitude enhancement in Signal-to-noise ratio (SNR) compared to conventional 5 mm probes has been demonstrated in a solenoid containing a 5 nL sample [3]. ^{1}H-NMR on picoliter-scale sample volumes in biological cells has been demonstrated using a 267 µm diameter solenoid [8]. Furthermore, planar microcoils, patterned by means of micromachining methods on fluidic chips have shown their feasibility for the analysis of minute biological samples [9] and for monitoring of chemical reactions in situ [10,11].

A short-coming of many existing micro-NMR systems is their limited spectral resolution, which in most cases does not comply with the state-of-the-art high-resolution NMR standard. Since one is aiming for high-sensitivity, the coil is positioned close to the sample. However, in general the coil metal has another magnetic suscep-

tibility than the sample, resulting in $B_0$-inhomogeneities over small distances, which hardly can be counteracted by shimming. High resolution is the cornerstone of the NMR technique because this provides the superb chemical specificity and molecular structure information. In order to maintain optimal resolution, the coil has to be either placed further away from the sample, which compromises sensitivity, or immersed in a susceptibility-matching fluid [4], which severely adds to the complexity of the design.

Recently we have introduced a new coil design, based on a stripline configuration [12–14]. By utilizing the stripline geometry as a detection coil in a microfluidic device, the trade-off between resolution and sensitivity is by-passed. The stripline has the advantage that positioning the coil close to the sample does not decrease the resolution [12]. A slightly different approach was taken by Maguire and co-workers, who used a small slot in a microstrip waveguide to generate high rf-fields in small volumes [7]. Microslot based resonators bear common ideas with the stripline, although ground planes are absent. The approach proved to be useful for metabolic studies on very small samples [15].

In a previous study [9,10] we have compared the resolution and sensitivity of solenoids, planar coils and striplines. We have also shown the feasibility of stripline flow-probes for the kinetic monitoring of chemical reactions and the analysis of 600 nL of human cerebrospinal fluid (CSF) [11]. In the present paper, an optimization study in terms of rf-homogeneity, resolution and sensitivity will be presented and compared to the NMR performance of our microfabricated fluidic device.

### 1.1. Principle

Generally, when a radio frequency (rf) current is fed through a straight wire, an electromagnetic rf-field will be generated which
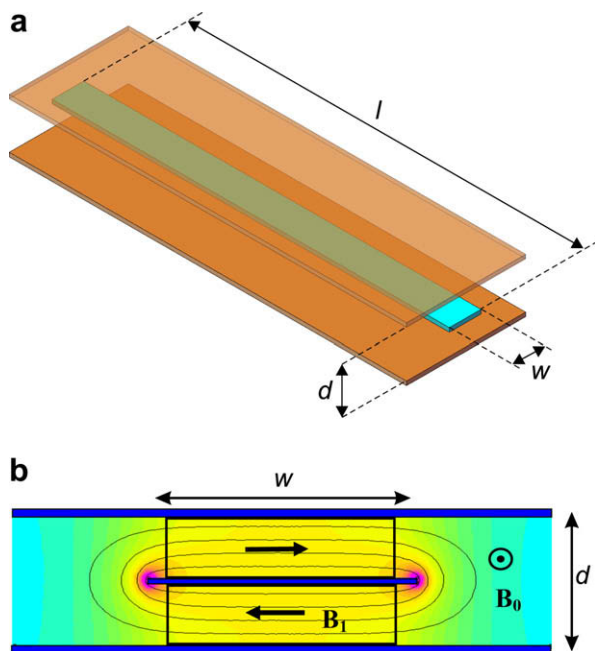
---

* Corresponding author. Fax: +31 53 489 4683.
  E-mail address: j.g.e.gardeniers@utwente.nl (J.G.E. Gardeniers).

encircles this wire. When such a wire is positioned parallel to a static $B_0$-field, the generated magnetic component of the rf-field is perpendicular to this static field, and can be used for the excitation of NMR transitions. This simple 'coil' geometry is very interesting because it hardly disturbs the static field homogeneity, essential for high-resolution NMR spectroscopy. From Maxwell's equations, it can be deduced that an infinitely long metal wire placed parallel to a static magnetic field does not affect the homogeneity of this field. This approximately holds also for finite length wires, as long as the length of the wire is much larger than the distance of the sample from this wire.

Our stripline probes are a 2D analogue of such a wire. The current is fed through a flat copper strip. Clearly a simple flat strip is not an efficient NMR detector as the rf-field strength decays inversely proportional with the distance to the strip. For that reason, ground planes are applied above and below the central strip which help to homogenize the rf-field. Fig. 1a shows a schematic representation of the geometry, indicating the dimensional parameters, *l* (length of the strip), *w* (width of the strip) and *d* (distance between the ground planes). The rf-current is fed through the central strip, and the rf-field generated by this current encircles the strip, (Fig. 1b). Because of the applied ground planes, a confined volume exists with a homogeneous $B_1$-field and a high filling factor can be achieved. Sample chambers can be positioned above and below the central strip as indicated by the black boxes in Fig. 1b. The resulting structure is optimal for high resolution and high sensitivity NMR, because of the minimal susceptibility distortion combined with the high filling factor.

### 1.2. Lab-on-a-chip implementation

The 3D structure of a stripline, shown in Fig. 1 was aimed to be implemented as a fluidic Lab-on-a-Chip utilizing common microfabrication technology. For reasons of fabrication simplicity, a con-

struction based on two substrates was chosen, one carrying the central strip and one containing a single fluidic channel. Ground planes were applied on the backsides of both substrates resulting in the configuration shown in Fig. 2.

In regular NMR probes the rf-coil is implemented as an inductive element (L) in an LC resonator. This means, that discrete elements have to be soldered to the rf-coil. Striplines offer the possibility to be designed as self-resonant structures, which makes the need for soldering of external electronics oblete. When the central strip is designed with a $\lambda/2$ length corresponding to the Larmor frequency of the nuclei to be observed, a standing wave as shown in Fig. 3a can be excited in the line. The current is maximum in the middle of the strip where it has a constriction, which increases the local current density resulting in a high rf-field at the position of the sample (Fig. 3b). The transition from the constriction to the so-called wide zone is designed with a taper for reasons discussed below.

Since the coil is used both for excitation and detection, the effective signal contribution as a function of the position along the channel shows that the sample at the position of the constriction dominates the detected signal. Fig. 4 shows an exploded view of a self-resonant stripline according to the description above.
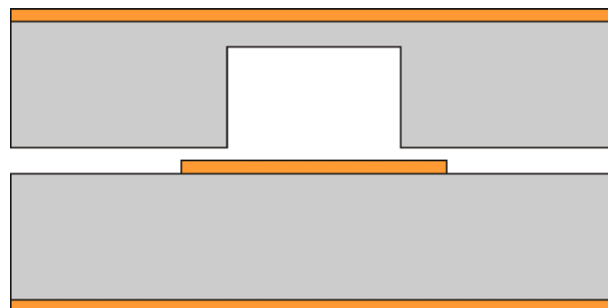
### 1.3. Substrate choice and modification

We aimed for an NMR chip which could be fabricated by means of common microfabrication technology. For the NMR detector described here, silicon was used as a substrate. Silicon is an absolute proton-free substrate, which assures flat baseline spectra without any background resonances. Furthermore, a very wide manufacturing infrastructure for silicon fabrication exists which makes fabrication of this chip, as well as future integration with electronic or microfluidic functionality straightforward. Finally, the high dielectric permittivity $\varepsilon_r$ of silicon limits the total length of the chip when it is designed as a $\lambda/2$ resonator. Eq. (1) gives the wavelength $\lambda$ of an electromagnetic wave with frequency *f* propagating through an ideal transmission line [16]:

$$\lambda = \frac{v}{f} = \frac{c}{f\sqrt{\mu\varepsilon}} \qquad (1)$$

where *v* is the propagation velocity, *c* is the speed of light in vacuum, $\mu$ the magnetic susceptibility of vacuum $\mu_0$ multiplied by the susceptibility of the substrate $\mu_r$, and $\varepsilon$ the dielectric permittivity of vacuum $\varepsilon_0$ multiplied by the dielectric permittivity of the substrate $\varepsilon_r$.

Using a semi-conducting material as a substrate is not trivial considering the high frequencies at which $^1$H-NMR usually operates (300–1000 MHz). Free charge carriers present in the standard bulk silicon contribute significantly to the total losses of the detec-



**Fig. 1.** (a) 3D representation of a stripline configuration. Color differences are only for clarity: the central strip which feeds the rf-current and the ground planes are made from the same material. Typical dimensional parameters are shown. (b) Cross-sectional field pattern of a stripline. The field pattern is homogeneous, except for the field around the very edges of the strip. (From Ref. [12]). (For interpretation of the references to colour in this figure legend, the reader is referred to the web version of this article.)



**Fig. 2.** Lab-on-a-chip implementation based on two substrates. The central strip is defined on the bottom substrate and the sample chamber in the top substrate. Ground planes are defined at the backsides of both substrates. Clearly, for a working device these two substrates have to be merged to achieve a leak-free structure.
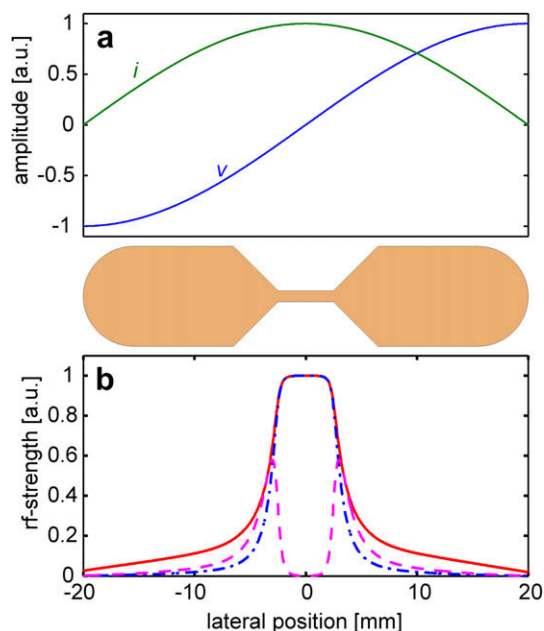
**Fig. 3.** (a) The standing wave pattern excited on a $\lambda/2$ stripline resonator. The lateral current ($i$) and voltage ($v$) distribution. (b) The lateral rf-field (solid red line, numerically determined) and the lateral signal intensity after a 90° pulse (blue dash-dot line). The constriction clearly enhances the local current density. Because of the finite diameter of the wide zone and more importantly the tapering, a residual signal after a 180° pulse is visible (purple dashed line). (For interpretation of the references to color in this figure legend, the reader is referred to the web version of this paper.)
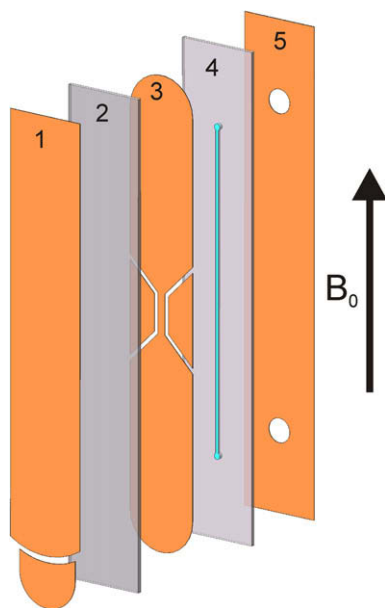


**Fig. 4.** Exploded view of a $\lambda/2$ stripline-based NMR chip. Layer 1: grounded copper plane. The small separated area on the bottom side represents the capacitive coupling to the external electronics. Layer 2: substrate. Layer 3: central line feeding the rf-current. A constriction is defined by removal of narrow copper lines. The remaining trapezoidal shaped copper areas are electrically isolated. Layer 4: substrate containing a microfluidic channel. Access-holes are in the backside. Layer 5: grounded copper plane with microfluidic access-holes.

tor. This is especially the case for a stripline configuration where the electrical field component of the rf-wave is perpendicular to the substrate. Substrate-induced losses are usually denoted by

the loss factor tan $\delta$, which is inversely proportional to the quality factor $Q$ (tan $\delta$ = $1/Q$). The loss factor of bulk silicon can be split in tan $\delta_C$ which is the contribution of the conductive losses caused by the finite resistivity of the substrate, and tan $\delta_P$ which is defined as the polarization loss caused by ionic and electronic polarization [17–19]:

$$\tan\delta = \frac{\sigma}{\omega\varepsilon_0\varepsilon_r'} + \frac{\varepsilon_r''}{\varepsilon_r'} = \tan\delta_C + \tan\delta_P \qquad (2)$$

where $\sigma$ is the substrate conductivity, $\omega$ is the angular frequency and $\varepsilon_r'$ and $\varepsilon_r''$ are the real and imaginary parts of the dielectric permittivity, respectively. For ideal dielectrics having a very low $\sigma$, the first term is negligible and the losses are determined by the complex permittivity only. However, the abundant free charge carriers in silicon make tan $\delta_C$ dominant up to high frequencies, and tan $\delta_P$ begins to dominate in the high GHz range. To keep tan $\delta_C$ minimal, high-purity silicon with a minimal amount of free charges was used.

Apart from the losses induced by bulk-conductivity, surface losses have to be considered. At the interface between the silicon and an insulating layer (e.g. oxide), a charge accumulation layer (also called a surface channel) is formed due to dangling silicon bonds and fixed charges in the $SiO_2$ [20–24]. The amount of accumulated charge is about an order of magnitude larger than the total amount of mobile charge present in the bulk [22], which makes this layer very conductive and thus lossy. The surface conductivity can be decreased by making the substrate surface amorphous, thereby decreasing the carrier mobility. Amorphous silicon ($\alpha$-Si) can be deposited by means of plasma enhanced chemical vapour deposition (PECVD) [23] or low pressure chemical vapour deposition (LPCVD) [24]. Another approach to achieve a damaged crystal structure is the implantation of high energetic argon ions in the substrate [20–22]. All these methods have proved effective in suppressing surface losses, making the bulk-induced loss mechanism dominant. By using a high resistivity silicon substrate (to minimize bulk silicon induced losses) and surface amorphisation (to minimize the surface channel losses), silicon can therefore be made suitable for rf-applications.

### 1.4. Computational modelling and optimization

The performance of an NMR detector is commonly expressed in three entities: the rf-homogeneity, the spectral resolution and the sensitivity. The dimensional ratios ($w/d$ and $l/w$) of the detector influence these entities and can be optimized. For the stripline, our strategy was to aim for a maximum sensitivity for a specified rf-homogeneity maintaining the optimal resolution. A further requirement is that the design should be manufacturable, that is, fabrication limitations were taken into account.

#### 1.4.1. rf-homogeneity

A high rf-homogeneity is of importance for complex spin manipulations based on successive 90° pulses along different axes. When the rf-field is inhomogeneous, not every spin gets the same tip angle, which means that after a few pulses the magnetization is scrambled which affects the final SNR. Usually, the rf-homogeneity is determined by means of a so-called nutation experiment, in which the signal amplitude is recorded for increasing pulse lengths. The ratio of the signal amplitudes after an 810° and a 90° pulse ($A_{810°}/A_{90°}$ ratio) is a common measure for the rf-homogeneity. Commercial liquid-state probes based on saddle-coils show $A_{810°}/A_{90°}$ ratios on the order of 80%. This value is adopted as a starting point for our optimization procedure.

Nutation can be very well predicted using finite element methods for the representation of the generated rf-field. The cross-sec-

tional rf-field distribution at the centre of the constriction was computed using finite element methods for magnetics (FEMM) [25]. Typical pictures are shown in the insets of Fig. 5a.

Simulations were performed for varying stripline width with respect to the distance of the ground planes, expressed as $w/d$. Small $w/d$ values are expected to yield a low homogeneity (and with that a low filling factor) because they approach a circular wire which intrinsically has a low homogeneity. This is in agreement with the simulations shown in Fig. 5a, which predict a decrease in effective filling factor (which we here define as the area where the rf-field is >80% of the maximum rf-field strength) for low $w/d$ ratios. In the insets, the sample chambers are indicated with black boxes.

It has to be noted that these simulations are valid for every size of the detector, as long as the aspect ratio $w/d$ is kept constant. From this graph it is concluded that the $w/d$ ratio should be maximized to obtain the best rf-homogeneity. However, for small sample volumes (below 1 μL) the $w/d$ ratio is limited by fabrication possibilities; too low $w/d$ ratios lead to impractical designs because extremely thin substrates have to be used. Practical numbers for $w/d$ are considered to be between 1 and 1.5.

The rf-homogeneity was also modelled for the specific construction based on two substrates (Fig. 2). In this design the sample is positioned directly on top of the central line. Substrates of 0.5 mm thickness were used in which a channel was etched with a width of 400 μm and a depth of 300 μm. The stripline width was 1 mm, resulting in a $w/d$ of 1.

For fabrication reasons, this channel was kept rather narrow compared to $w$, resulting in a moderate filling factor, however, with a simulated $A_{810°}/A_{90°}$ ratio (cross-sectional) of 90%.

Apart from cross-sectional rf-inhomogeneities, lateral inhomogeneities were studied based on 3D rf-data sets, obtained by simulations in CST Studio Suite [26]. First, a sample plug with $0.75\times$ the length of the constriction and a diameter as indicated in Fig. 2 (channel width of 400 μm and depth of 300 μm) was examined for different constriction lengths. Since the rf-field is fairly homogeneous across this region (as indicated by Fig. 3b) the simulated $A_{810°}/A_{90°}$ ratio was maintained well above 90% for all studied lengths, see Fig. 5b. This means that for plug-flow applications, a simple rf-homogeneity prediction based only on the cross-section of the channel is sufficient. For completely filled channels, the simulated $A_{810°}/A_{90°}$ ratio decreased, because of the sample regions under the tapering which experience a weaker rf-excitation. For a sample with the same length as the whole central line the $A_{810°}/A_{90°}$ ratio decreases more rapidly for shorter constrictions. This is logical since the relative impact of the tapering is more dominant. For a constriction length of $5 \times w$, an rf-homogeneity of 78% was calculated for the design of Fig. 2.

### 1.4.2. Sensitivity

As has been stated by Hoult and Richards, the signal-to-noise ratio (SNR) of an NMR experiment scales according to [27]:

$$SNR \approx \frac{(\frac{B_1}{i})}{\sqrt{R}} \tag{3}$$

where $B_1/i$ is the rf-field generated per unit current and $R$ is the total resistance of the detector. Assuming a proper rf-homogeneity (in our case above 80%) $B_1/i$ and $R$ are determined by the ratio of the length and width of the constriction, $l/w$. Therefore, for a given sample volume and a fixed $w/d$ ratio (being 1 in our case) the optimal sensitivity can be found by varying the $l/w$ ratio. An optimum (taking the tapering resistance into account) was found for an $l/w$ ratio ~5 to 10, as shown in Fig. 6.

For a steeper tapering (towards 90°) the maximum is higher and shifts to the left. Therefore, a steeper tapering gives a better sensi-
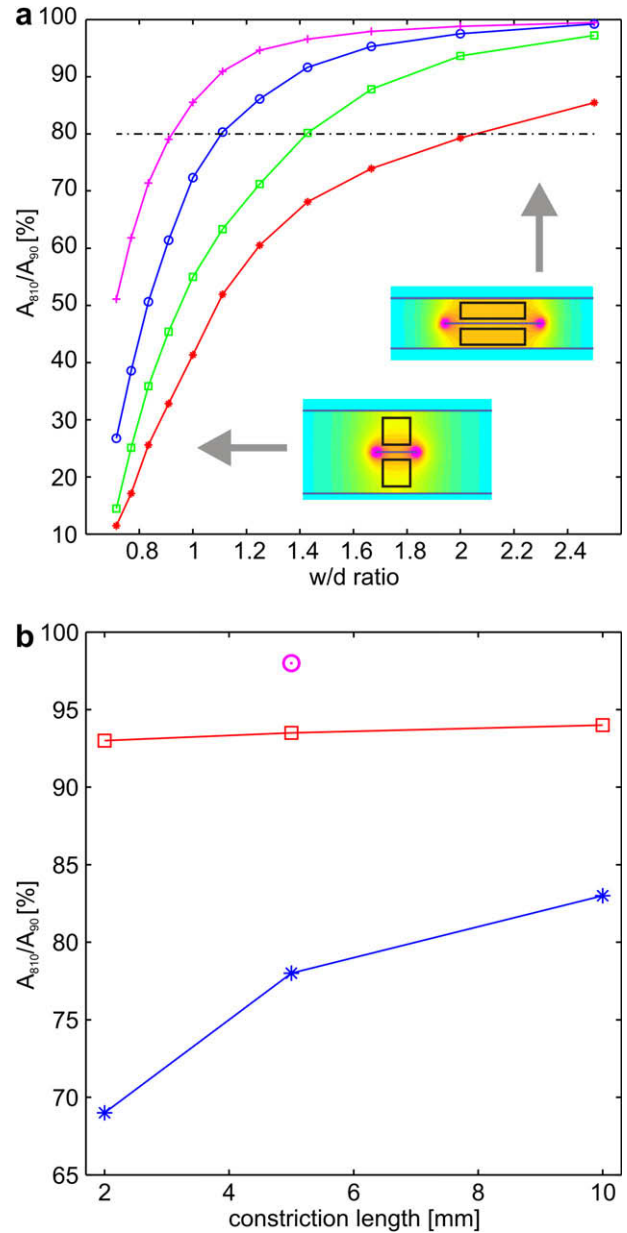


**Fig. 5.** (a) $w/d$ ratio dependence of the rf-homogeneity for four different effective filling factors. An effective filling factor of 100% corresponds to a sample size of $w \times d$. The black boxes were scaled equally in both dimensions. Purple line (+): sample size = $0.55w \times 0.55d$, filling factor = 30%. Blue line (○): sample size = $0.67w \times 0.67d$, filling factor = 45%. Green line (□): sample size = $0.77w \times 0.77d$, filling factor = 60%. Red line (*): sample size = $0.87w \times 0.87d$, filling factor = 75%. The insets give an indication of the geometry for the extremes of the $w/d$ ratios in the graph. For clarity reasons, only the $0.67w \times 0.67d$ sample area is shown, which has an $A_{810°}/A_{90°}$ ratio of 80% for $w/d = 1$. (b) Effective rf-homogeneity for a finite length sample plug centred on the stripline as indicated by Fig. 2, ($w/d = 1$, channel depth = 300 μm, channel width = 400 μm, constriction length = 5 mm). The red line (□) shows the data for a rectangular plug of $0.75 \times$ the length of the constriction, the blue line (*) represents the data for a sample as long as the whole stripline and the purple dot (○) is the rf-homogeneity for a cylindrical sample plug with a length of 3.75 mm (0.75 × the length of the constriction) and a diameter of 100 μm (see text for details). (For interpretation of the references to color in this figure legend, the reader is referred to the web version of this paper.)

tivity, however, is disadvantageous in terms of susceptibility broadening (see for motivation the resolution section below). In our implementation a tapering angle of 45° was chosen and the total length was set by the resonance condition (48 mm, see below). With these settings an optimal $l/w$ of 5 was found.
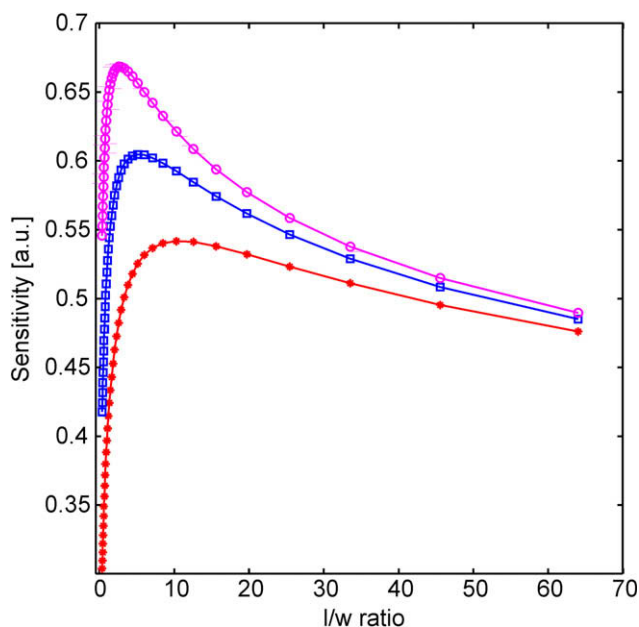
**Fig. 6.** Sensitivity as a function of the *l/w* ratio. Tapering and wide zone are taken into account. Red line (*): tapering 25°. Blue line (□): tapering 45°. Purple line (○): tapering 65°.

### 1.4.3. Resonance condition

As mentioned earlier, the length of the stripline determines the length of the standing wave that can be excited in the stripline. The length must be adjusted very carefully in order to make the chip compatible with a chosen Larmor frequency. Although calculations and simulations with lumped element electrical circuit models were performed in which the bulk induced losses were implemented, it turned out to be extremely difficult to predict the resonator length with a sufficient precision. Accurate size parameters had to come from 3D numerical simulations, which were performed based on the optimized parameters described before. For these simulations, all the optimized parameters in the 3D geometry were fixed and the total length of the central line was iteratively varied until the proper resonance frequency was found. Using this method, for a stripline with a constriction of $1 \times 5$ mm ($w \times l$), a tapering of 45° and a wide zone width of 9 mm, filled with an aqueous sample, the self-resonance length for 600 MHz was calculated to be 48 mm for a stripline on a silicon substrate. It must be mentioned that the resulting stripline would resonate at exactly 600 MHz, only for an aqueous sample. Other solvents, having another $\varepsilon_r$ change the effective $\varepsilon_r$ of the dielectric and with that the resonance frequency.

### 1.4.4. Resolution

Since the stripline is positioned parallel to the static field ($z$-axis), minimal susceptibility broadening is expected. Nevertheless, magnetic susceptibility transitions along the $z$-axis such as the ends of the fluidic channel and the edges of the tapering will limit the final resolution. In order to study these effects, calculations were performed using a C-programmed numerical solver. The 3D geometry of the chip, consisting of the stripline and the fluidic channel, was defined in a static homogeneous field. The non-patterned substrate and ground planes were left out of consideration since they are very large compared to the sample and therefore have negligible influence on the susceptibility broadening. The whole 3D-space was divided in finite element sections which each were defined as dipoles having their own specific material properties. The lineshape was predicted by summing the effects of all the

dipoles in the 3D-space for every position in the channel. With these simulations, the crucial design parameters influencing the susceptibility broadening were studied. Fig. 7 shows which parameters are varied.

Fig. 8a shows the predicted NMR lineshapes for different channel lengths. Apparently, shortening the channel has a negative effect on the linewidth. This is caused by the magnetic permeability change at the ends of the channel, from that of the sample (e.g. water) to that of silicon. Therefore, the channel should be long compared to the constriction to keep these distortions far away from the detection area. When there is no practical limitation, the best is to design the fluidic in- and outlets close to the edge of the chip, as we have done in the current implementation.

It was found that a tapering angle $\alpha$ of 90° exhibits maximum sensitivity. However, such an angle means a sudden discontinuity, resulting in a $B_0$-gradient in the channel above the constriction. Low values for $\alpha$ are therefore advantageous in terms of resolution, but will lead to a decrease in sensitivity and a poor sample selection. Therefore, we compromised choosing an angle of 45°.

Earlier simulations have shown that for a simple copper structure without any susceptibility matching the distortion of the $B_0$-field could be limited to below 0.1 ppm [12]. The main cause for the $B_0$-field distortion was found to be the tapering, being designed by removal of all the copper around the constriction (as schematically shown in Fig. 3). To limit this susceptibility broadening, one has to realize that it is not necessary to remove all copper to construct the narrow strip section. Starting from a uniform strip without a constriction, one can make a constriction by defining a gap as shown in Fig. 7. Such a design effectively routes the rf-current in the narrow constriction, but leaves nearly all the copper, which means a minimal deviation from a long uniform strip. Fig. 8d compares the local field variations of a stripline which is defined by removal of all the copper around the constriction, and one which is defined by a gap. Clearly the local field variations can be minimized by such an approach.

The $B_0$-field distortion can be minimized further by filling the gap with a material having a susceptibility closely matching that of copper ($\chi_{Cu} = -9.60E{-}6$), as shown in Fig. 8b. Of course, for the choice of this filling one is limited to proton-free materials like
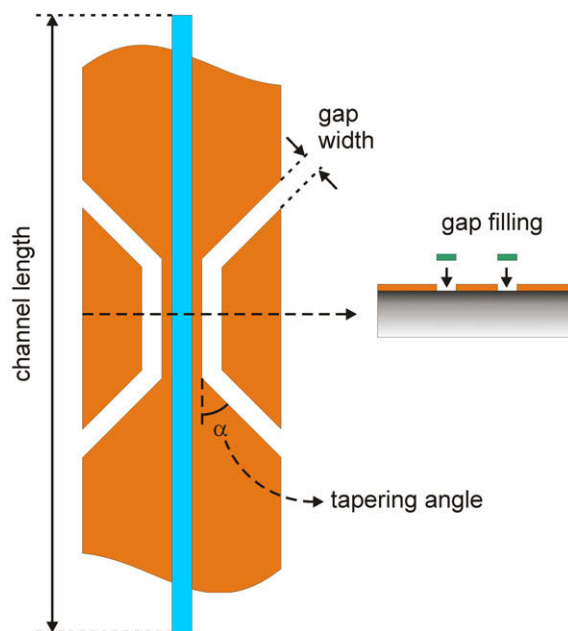


**Fig. 7.** Parameters which are varied for optimization of the resolution. In the text, these parameters are described in detail.
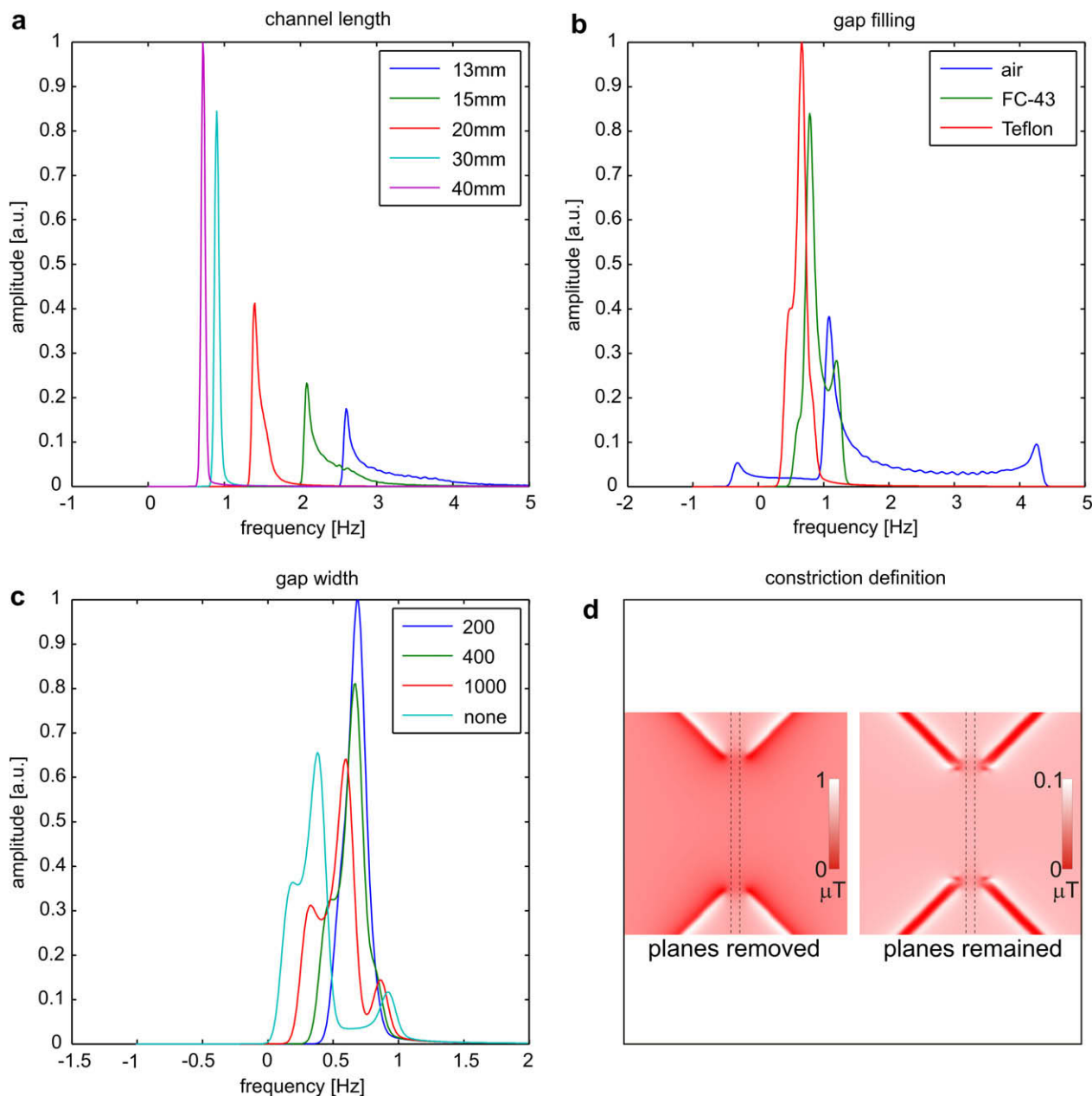
**Fig. 8.** (a) Predicted line shapes for channel length variations. Distortions caused by the copper structure are cancelled, to visualize only channel length effects. (b) Predicted line shapes for gap material variations. The channel length is set to 40 mm and the gap width to 400 μm. (c) Predicted line shapes for gap width variations. The channel length is set to 40 mm and the gap is filled with FEP (see text). (d) 2D simulation of the local field variations in a plane 150 μm above the central strip for a constriction defined by removal of all the copper around it (left), and defined by a gap (right). The channel is indicated with dashed lines. The $B_0$-field distortion along the channel defined by a gap is lower than the one defined by removal of all the copper. Note the scale difference in both pictures.

fluorocarbons. Furthermore, since a fluidic susceptibility matching material is not easily implemented in the current design, we prefer a solid film. Fortunately, the susceptibility of Polytetrafluoroethylene (PTFE) is close to that of copper ($\chi_{PTFE} = -10.5E-6$ differs only 9.4% from $\chi_{Cu}$) [28]. Fluorinated ethylene propylene (FEP) is expected to have almost the same $\chi$ and is available as a thin foil. For comparison, the effect of the well-known FC-43 susceptibility-matching fluid ($\chi_{FC-43} = -8.23E-6$ differs 14.3% from $\chi_{Cu}$) [4] is also shown, which exhibits similar results.

Fig 8c shows that a decrease in gap width results in a higher resolution. This is in agreement with expectations since the discontinuities decrease in size. On the other hand, the sensitivity is negatively affected by a decrease in gap width, because of enhanced eddy-currents induced by the central line in the isolated copper planes. The optimal gap width, for which the SNR in the frequency domain is maintained and the resolution is maximized, is found to be between 200 and 400 μm. This result is based on a gap filled with FEP. With these settings, the susceptibility broadening is calculated to be below 0.5 Hz at 14.1 Tesla.

## 2. Experimental results

A microfluidic chip as schematically displayed in Fig. 4 was fabricated on two silicon substrates which were treated in order to minimize losses. The optimal dimensional ratios described above ($w/d = 1$ and $l/w = 5$) were adopted in this implementation, as well as the optimal results obtained from the susceptibility broadening simulations (gap width of 400 μm and gap filled with FEP).

## 2.1. Electrical performance

The substrates were investigated with respect to dielectric losses in a home-built low-loss LC resonator, in which the substrate was introduced as a dielectric. Since the losses of the inductor (L) in this device were minimized, the measured losses could be attributed to the substrate only.

Before α-Si deposition the substrates were tested, but no resonance could be established, indicating high losses at the surface. After passivation (by means of an LPCVD process), resonance could be obtained with a Q-factor of 37, which is equivalent to a tan $\delta$ of 0.027. This is in very good agreement with the value calculated for our particular system operating at 600 MHz. Using Eq. (2), a value for tan $\delta_C$ of 0.025 ($\varepsilon'_{r\,Si}$ is 11.9) was calculated. The α-Si passivation layer was also examined by X-ray diffraction (XRD). These measurements showed no diffraction lines, indicating an amorphous morphology.

## 2.2. rf-homogeneity

The results of the nutation simulations were experimentally verified. First, the whole chip was filled with a 100% ethanol sample. Fig. 9a shows a sequence of spectra, recorded with different pulse widths. From this, an $A_{810°}/A_{90°}$ ratio of 76% was measured, which is in excellent agreement with simulations that predicted 78%. To get rid of the signal contributions from the sample section under the tapered area of the stripline, a 40 mm fused silica capillary (100 µm ID, 200 µm OD) was filled with a 3.75 mm plug of 100% ethanol and restricted between two Fluorinert (FC-40) plugs of 15 mm length. For such a small sample volume, an $A_{810°}/A_{90°}$ ratio of 98% was predicted (purple dot in Fig. 5b). The capillary was positioned in the chip, such that the ethanol plug was symmetrically positioned under the 5 mm long constriction, whereafter the nutation experiment was run again. Fig. 9b shows the nutation plot for this experiment, from which an $A_{810°}/A_{90°}$ ratio of 99% was obtained, again completely according to the simulations.

## 2.3. Limit of detection

The limit of detection (LOD) and normalized limit of detection (nLOD$_m$) of this probe for 1D $^1$H-NMR were examined by the measurement of pure isopropanol and 600 nmol Sucrose, respectively.

We define the limit of detection (LOD) as the number of spins that have to resonate in a 1 Hz bandwidth to give a signal as strong as the noise in single acquisition:

$$LOD = \frac{N_s}{SNR_{t,SS}\sqrt{\Delta f}} \qquad (4)$$

where $N_s$ is the number of spins, $\Delta f$ is the bandwidth in which the spins resonate (the linewidth of the particular line) and $SNR_{t,SS}$ is the single scan SNR in the time domain. Determination of the LOD must be performed with a sample having a well-known proton concentration (without unknown proton residues from e.g. D$_2$O). In that case, the first point in the Free Induction Decay (FID) corresponds to the integral of all the protons in the sample, and gives a reliable $SNR_{t,SS}$.

A four times averaged pure isopropanol (3.8 × 10$^{19}$ spins in 600 nL) spectrum, shown in Fig. 10, yielded an LOD of 2.8·10$^{14}$ spins/$\sqrt{\text{Hz}}$ (0.47 nmol/$\sqrt{\text{Hz}}$). The LOD of this chip could be predicted using the numerically determined $B/i$ and a calculated $R$ (including tapering and wide zone) as described before [12]. Assuming only copper losses and neglecting the substrate losses an LOD of 3.1 × 10$^{13}$ spins/$\sqrt{\text{Hz}}$ was predicted for this structure. As no other sources for signal loss are obvious, it must be concluded that the substrate-induced losses decrease the LOD with a factor of 9.
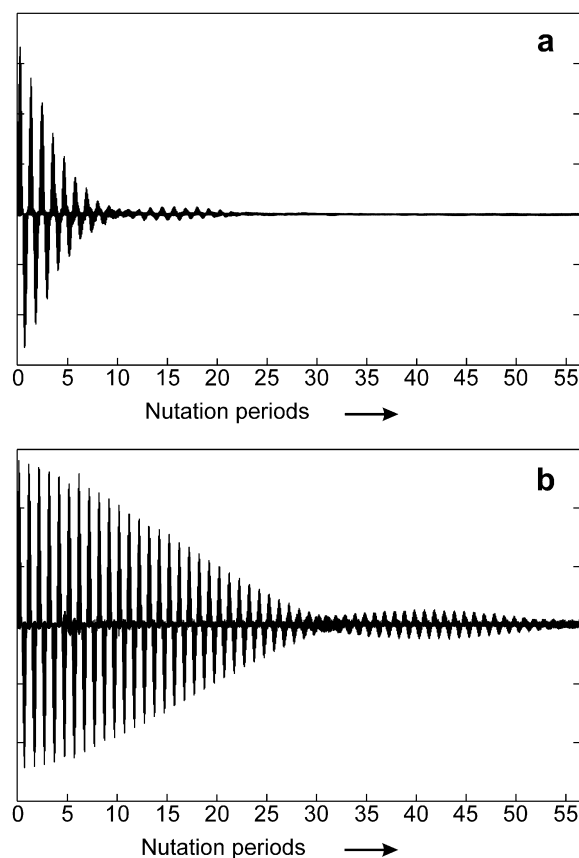


**Fig. 9.** Proton nutation signal of pure ethanol (methyl signal) at 600 MHz for different sample geometries. (a) Complete channel (300 × 400 × 5000 µm) filled with pure ethanol. $A_{810°}/A_{90°}$ ratio is 76%. An $A_{810°}/A_{90°}$ ratio of 78% was simulated, see Fig. 5. (b) A 3.75 mm plug of pure ethanol encapsulated in between two 15 mm long fluorinert plugs in a 4 cm long fused silica capillary (ID 100 µm, OD 200 µm) positioned in the same channel (Fig. 10a) such that the plug is centered on the 5 mm long constriction. The $A_{810°}/A_{90°}$ ratio is 99%. An $A_{810°}/A_{90°}$ ratio of 98% was simulated, see Fig. 5b.
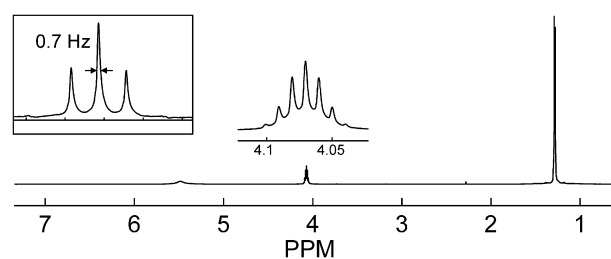


**Fig. 10.** 4 times averaged unapodized $^1$H-spectrum of pure isopropanol. The SNR$_t$ was 3839 from which an LOD of 2.8 × 10$^{14}$ spins/$\sqrt{\text{Hz}}$ (0.47 nmol/$\sqrt{\text{Hz}}$) was calculated. The linewidth (after coarse shimming) is 1.9 Hz, as determined with a Lorentzian fit on the multiplet. The inset shows the methyl peak of a $^1$H-spectrum of pure ethanol after careful shimming. The linewidth is 0.7 Hz, as determined with a Lorentzian fit.

For convenient comparison with other micro-NMR systems, we also measured 600 nMol Sucrose and determined the nLOD$_m$ [15,29]. The nLOD$_m$ is defined as the mole quantity necessary to obtain an SNR of 3 for a specified resonance peak in one second. We prefer the LOD of Eq. (4) over the nLOD$_m$ because this definition makes comparison of different probes straightforward, since it is independent of the data treatment and sample in contrast to nLOD$_m$.

Fig. 11 shows the single scan spectrum obtained after 1.5 s water-suppression. The SNR (defined as the height of the peak of
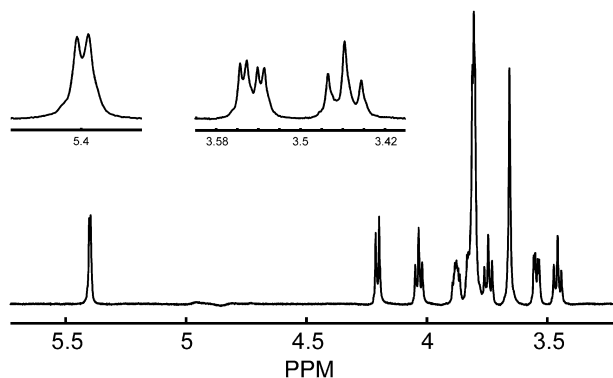
**Fig. 11.** Single scan unapodized $^1$H-spectrum of 600 nmol Sucrose in $D_2O$. Pulse delay: 3 s; Water suppression by pre-saturation: 1.5 s at a power of 1 μW (-16 dB); 90° pulse: 3.7 μs at a power of 5 W (53 dB); acquisition time: 1 s; spectral width: 1.5 kHz. Total time per scan: 5.5 s. The SNR of the anomeric proton doublet was 189. The insets show details of the spectrum which indicate the superior resolution. Small J-couplings of 3.67 Hz are clearly resolved.

interest divided by 2 times the root-mean-square of the noise) for the anomeric proton of sucrose was 189. The $nLOD_m$ was calculated to be 22.3 nmol·$\sqrt{s}$. Since the measurements were performed on a 600 MHz system, scaling was not necessary. To compare this number with the results of Krojanski et al. [15], who reports an $nLOD_m$ of 0.39 nmol·$\sqrt{s}$ for 10.6 nL, our $nLOD_m$ was scaled to the same volume of 10.6 nL (57 times smaller). Decreasing the sample volume with a factor of 57 gives a sensitivity increase [27] of $57^{(1/3)}$ yielding an $nLOD_m$ of 5.8 nmol·$\sqrt{s}$. Again, this lower sensitivity is attributed to the substrate-induced losses and the non-optimized filling factor.

## 2.4. Shimming and resolution

From the linewidth broadening simulations discussed above, it was predicted that our design could exhibit a linewidth of <0.5 Hz. In these simulations, the susceptibility distortions of the probe housing were not taken into account. These distortions, caused by the materials used for the probe were expected to be easily compensated with the standard shim set. However, the applicability of the standard shim set is rather limited for the tiny samples handled on chip. Because the chip-induced distortions were concentrated in a very small volume, extremely accurate settings for higher order shims were demanded. It was indeed observed that sharp lines are easily obtained by coarse settings of $Z1$, $Z2$, $X$ and $Y$ shims. Fig. 10 shows the spectrum of pure isopropanol after 5 min shimming. The J-multiplets are clearly resolved, and a linewidth of 1.9 Hz is measured. For an as perfect as possible shim, which required careful and long time shimming, a linewidth of 0.7 Hz (1.2 ppb) for pure ethanol was achieved (Fig. 10, inset) which is close to the simulation results for this geometry, discussed above.

## 2.5. rf-strength

Although not of interest for proton NMR, the fact that microcoils can generate extremely high rf fields has a great potential for obtaining spectra of other nuclei with resonance lines that are dispersed over a bandwidth of several megahertz. Full excitation of such a spin system requires high rf-fields. The rf-strength as computed with the nutation data discussed above was 36 kHz at a source power of 5 Watt. This is in very good agreement with a simple model based on Ampere's law to predict the field strength around the strip combined with the experimentally determined Q-factor, giving an rf-strength of 35 kHz. Since the stripline is built

on a pure silicon substrate which is an excellent heat conductor, wider bandwidths (associated with higher powers) are readily accessible [12].

## 3. 2D spectroscopy

The 2D data acquisition ability of our detector (which relies on a good rf-homogeneity) was demonstrated with homo-nuclear proton Correlation Spectroscopy ($^1$H–$^1$H COSY). For this experiment, a 2 M glucose solution in $D_2O$ was prepared and loaded in the chip, such that the complete channel was filled. Fig. 12 shows the 1D and 2D plots as recorded with the stripline chip. All the expected resonance peaks and off-diagonal correlation peaks were clearly distinguishable with minimal phase cycling (4×).

This picture demonstrates that all parameters for high performance 2D NMR are at a proper level, and with that the chip (without special plug-flow operation) is applicable for the elucidation of complex molecules, from which the structure cannot be unravelled with 1D experiments.

## 4. Discussion

It was found that the stripline geometry can be modelled in detail and an optimization towards required sensitivity, good $B_1$-homogeneity and ultimate resolution is possible. Moreover, the experimental results are in excellent agreement with simulations, which implies that optimization for other sample sizes or geometries is straightforward. The implementation based on two substrates has turned out to be a useful platform for the evaluation of the stripline performance for NMR detection.

The stripline chip was based on a $\lambda/2$ resonator. The advantage of a $\lambda/2$ geometry is that it is a contactless resonator, preventing loss problems associated with contact resistance. Since the wavelength at 600 MHz is rather long (0.5 m in air and 0.33 m on a low-loss substrate like PTFE), we chose silicon as a substrate for its high $\varepsilon$ (11.9). Apart from that, silicon yields the possibility to implement extra functionality like (CMOS) pre-amplifiers.
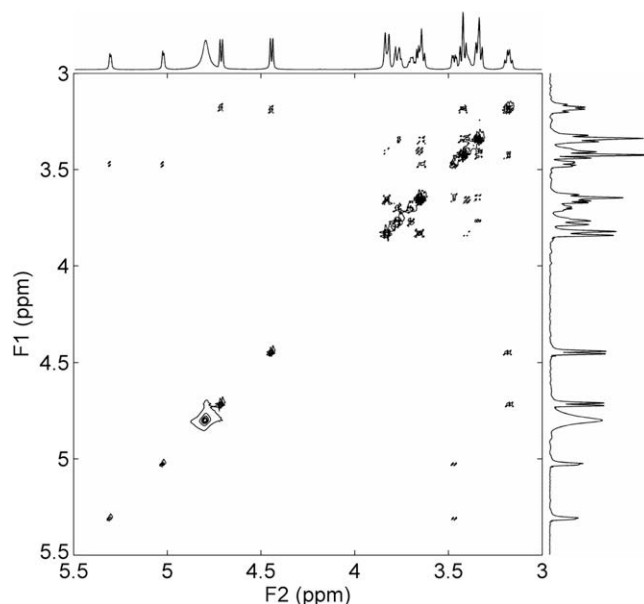


**Fig. 12.** Two-dimensional $^1$H-$^1$H COSY spectrum of 1.2 μmol $^{13}$C-labeled Glucose solution in $D_2O$ (2 M in 600 nL), obtained with the stripline probe. 1024 T1 increments with minimal phase cycling of 4 scans were taken. Acquisition time per scan was 2 s, and the pulse delay 10 s. The total measurement time was 13.6 h.

For low-loss substrates we have demonstrated that the predicted sensitivity for striplines very accurately complies with experimental results [12]. Therefore, a comparison of the predicted LOD based on negligible losses in the silicon substrate with the experimentally achieved LOD in this work clarifies that the lower sensitivity must be attributed to substrate losses. Actually, this is already expected from the moderate Q-factor which was obtained after implementation of the substrate as a dielectric in a low loss LC-resonator (see above). Therefore, although the substrate is treated to minimize losses, it turns out that the passivation was not sufficient to obtain an LOD close to the predicted value assuming a low-loss substrate.

Since sensitivity is essential for NMR, stripline probes designed on other substrates (e.g. fused silica implemented as a $\lambda/4$ structure) are worthwhile to be studied. Apart from that, the filling factor (which was not optimized in the current chip design) should be enhanced by fabrication of two channels on both sides of the central line. Such an optimized chip, with a higher filling factor and a low-loss substrate is currently under study.

## 5. Conclusions

We have modelled and built a stripline-based micro-NMR detector. The optimization of sensitivity, resolution and rf-homogeneity has been discussed. 2D and 3D rf-field simulation results were used for optimization of the stripline geometry. Optimal dimensional ratios of $1 < w/d < 1.5$ and $5 < l/w < 10$ were found. Experimental results were in excellent agreement with the simulation outcome. Nutation experiments gave an rf-homogeneity of 76% ($A_{810°}/A_{90°}$ ratio) for a completely filled channel whereas 78% was predicted. This number is comparable with commercial liquid-state NMR probes, and allowed for high-resolution 2D spectroscopy of $^{13}$C-Glucose. Based on NMR lineshape predictions a linewidth of 0.5 Hz was expected, and a linewidth of 0.7 Hz was found experimentally. An rf-strength of 36 kHz was reached for 5 Watt input power. The LOD of $2.8 \cdot 10^{14}$ spins/$\sqrt{Hz}$ was moderate compared to numbers reported in literature, which is attributed to electrical losses in the silicon substrate.

## 6. Experimental

### 6.1. Chip fabrication

The 300 μm deep channel and the in- and outlets were fabricated by means of Deep Reactive Ion Etching (DRIE) using a standard Bosch process with $SF_6$ as etch-gas and $C_4F_8$ for passivation [30] After etching the channel, the surface was protected with a foil, and patterned from the backside with holes for the in- and outlet. These were etched completely through, making the channel accessible from the outside.

The α-Si was deposited on all the wafers by a modified LPCVD method compared to the work by Klootwijk et al. [24]. Before deposition the wafers were successively cleaned in freshly prepared 100% $HNO_3$ (Selectipur: Merck) and 69% boiling $HNO_3$ (VLSI: Merck). Deposition was performed for 217 min at 550 °C with a $SiH_4$ flow of 25 sccm. The pressure was regulated to 1.0 mbar by $N_2$. After unloading, the wafers were immediately covered at both sides with $SiO_2$ by means of a PECVD process (300 °C, $SiH_4$ flow: 425 sccm, $N_2O$ flow: 710 sccm, pressure: 1.3 mbar). Both layers had a thickness of 500 nm as measured with a height profile measurement.

To define the copper structures, a 16 nm titanium adhesion layer and 200 nm copper seed layer were sputtered over the unpatterned wafer. Thick AZ9260 (Clariant, Wiesbaden, Germany) resist was lithographically patterned on the wafer with a thickness of 25 μm to define the copper structure. A dedicated electroplating set-up, based on Slotocoup HL10 bath chemistry (Schlötter GmbH, Geislingen, Germany) and a DμP(R)10-1-3 powersupply (Dynatronix Inc., Wisconsin, USA) operating in DC-mode, was utilized. 30 min plating at 1 A/dm$^2$ yielded a copper layer with a thickness of 10 μm (>3 times the skin depth of copper at 600 MHz). After the resist was removed, the remaining seed layer was removed by ion beam etching (IBE) to isolate the separate structures electrically. The ground planes were fabricated with the same process after bonding.

Bonding is the process in which the two wafers are merged together, such that they are leakage free and mechanically stable. Because of the α-Si layer and the copper stripline, bonding methods based on high temperatures like fusion bonding [31] and anodic bonding [32] were inapplicable. At first glance, intermediate layer bonding [32] is the most obvious wafer bonding technique for the stack described here. However, since most intermediates are hydrogen-rich polymers, the choice is severely limited by the chemical composition. A completely fluorinated polymer would be the optimal intermediate, but these molecules can not establish a covalent bond with the $SiO_2$ surface. For these reasons we have developed a new bonding method based on an intermediate layer as is described elsewhere [33]. As an intermediate, we used Fluorinated Ethylene Propylene (FEP 100A), a copolymer of hexafluoropropylene and tetrafluoroethylene, (DuPont, Sabic Innovative Plastics Snij-Unie, Enkhuizen, The Netherlands). FEP 100A film is a transparent thermoplastic with a thickness of 25 μm. Aligned bonding was performed on an EVG-620 mask-aligner in combination with an EV-501 anodic bonder. Both wafers were aligned with a FEP foil in between. During bonding, and a force of 100 N/cm$^2$ was applied for 14 h. It was observed that the applied force was enough to squeeze the FEP (which is deformable) in the gap around the constriction. This was necessary to obtain a proper susceptibility matching. The established bonds were strong enough to withstand the applied pressures (<2 bar).

### 6.2. Probe fabrication

Special attention was given to the symmetry and simplicity of the probehead. The top part of a long aluminum cylinder (ID 9 mm, OD 11 mm, length 60 cm) was divided in two halves. Small trenches of 0.5 mm deep were milled in both halves in which the 1 mm thick chip could be placed, resulting in a non-radiative cylindrical structure (Fig. 13a).

The return line connection was established by the direct contact between the copper shielding planes and the aluminum. This geometry keeps the holder metal far away from the sensitive area of the chip, warranting low influence on the $B_0$-homogeneity. Holes were drilled in the sidewalls of the cylinder to connect the microfluidic capillaries and the rf-contact (Fig. 13b).

The resonance frequency of the chip is intrinsically determined by the length of the stripline, and the lithographic accuracy of ~1 μm is sufficient to achieve the aimed sizes (a deviation of 1 μm corresponds to a resonance frequency deviation of 8.3 kHz). However, larger deviations will be induced by sample parameters like the dielectric permittivity and losses (Eq. (1)). For example, switching the sample solvent from water ($\varepsilon_r$ = 80) to chloroform ($\varepsilon_r$ = 4.8) gives a resonance shift of 12 MHz in this configuration. Therefore, external fine-matching and fine-tuning capacitors were connected. Fig. 13b and c show how this matching and tuning circuit is integrated schematically in practice.

### 6.3. Materials

Float zone High Resitivity Silicon (HRS) wafers with a resistivity of 10.000 Ω cm, a thickness of 525 μm and a diameter of 100 mm were purchased from Topsil, Denmark. 99.99% $D_2O$, ethanol (96% pro-analysis) and isopropanol (pro-analysis) were purchased from
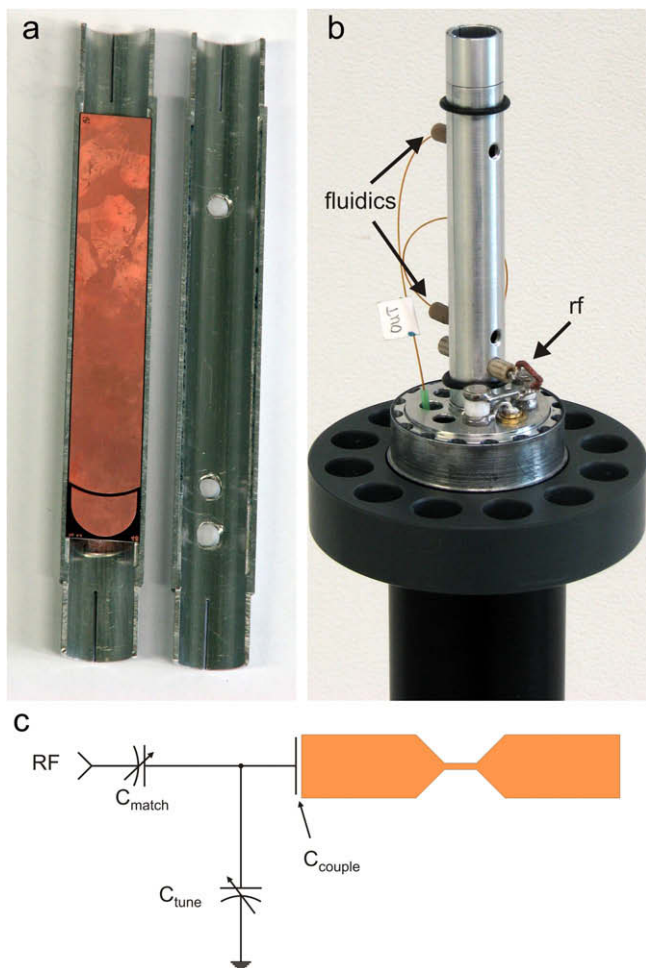
**Fig. 13.** (a) The two halves of the aluminum cylinder showing how the chip is mounted. (b) The probehead. The chip is positioned in an aluminum cylinder in which fluidic access-holes are drilled from one side and an rf access-hole is drilled from the other side. The matching and tuning circuit is placed on the horizontal platform close to the rf-connector. (c) Schematic representation of the rf-implementation. The stripline resonator is capacitively coupled to the rf-circuitry. The capacitance $C_{couple}$ is much larger than the matching capacitance $C_{match}$ so that the latter dominates the matching. Although the structure in principle resonates at the desired frequency a small tuning capacitor ($C_{tune}$) is included in the circuit to compensate for changes induced by the samples effective dielectric coefficient ($\varepsilon_r$).

Aldrich Chemical. 99.5% Sucrose was purchased from J.T. Baker (Deventer, The Netherlands). d-glucose-1-$^{13}$C was purchased from CAMPRO Scientific (Veenendaal, The Netherlands). All chemicals were used as received.

### 6.4. NMR experiments

The NMR experiments were carried out on a Chemagnetics CMX-Infinity 600 solid-state NMR spectrometer (600 MHz) operated by Spinsight software. All spectra were recorded at 300 K and processed by using the MatNMR processing package [34].

The capillary which was used for nutation of a sample plug was sealed with Delo photobond 4436 (Delo industrial adhesives, Germany).

### References

[1] D. Janasek, J. Franzke, A. Manz, Scaling and the design of miniaturized chemical-analysis systems, Nature 442 (2006) 374–380.
[2] J. West, M. Becker, S. Tombrink, Andreas Manz, Micro-total analysis systems: latest achievements, Anal. Chem. 80 (2008) 4403–4419.
[3] N.A. Wu, T.L. Peck, A.G. Webb, R.L. Magin, J.V. Sweedler, 1H-NMR spectroscopy on the nanoliter scale for static and on-line measurements, Anal. Chem. 66 (1994) 3849–3857.
[4] D.L. Olson, T.L. Peck, A.G. Webb, R.L. Magin, J.V. Sweedler, High-resolution microcoil 1H-NMR for mass-limited, nanoliter-volume samples, Science 270 (1995) 1967–1970.
[5] J.D. Trumbull, I.K. Glasgow, D.J. Beebe, R.L. Magin, Integrating microfabricated fluidic systems and NMR spectroscopy, IEEE Trans. Biomed. Eng. 47 (2000) 3–7.
[6] C. Massin, C. Boero, F. Vincent, J. Abenhaim, P.A. Besse, R.S. Popovic, High-Q factor planar microcoils for micro-scale NMR spectroscopy, Sens. Actuators A 97(8) (2002) 280–288.
[7] Y. Maguire, I.L. Chuang, S. Zhang, N. Gershenfeld, Ultra-small-sample molecular structure detection using microslot waveguide nuclear spin resonance, Proc. Natl. Acad. Sci. USA 104 (2007) 9198–9203.
[8] K.R. Minard, R.A. Wind, Picoliter 1H-NMR spectroscopy, J. Magn. Res. 154 (2) (2002) 336–343.
[9] N. Baxan, H. Rabeson, G. Pasquet, J.-F. Chateaux, A. Briguet, P. Morin, D. Graveron-Demilly, L. Fakri-Bouchet, Limit of detection of cerebral metabolites by localized NMR spectroscopy using microcoils, C.R. Chimie 11 (2008) 448–456.
[10] H. Wensink, F. Benito-Lopez, D.C. Hermes, W. Verboom, H. Gardeniers, D.N. Reinhoudt, A. Van den Berg, Measuring reaction kinetics in a lab-on-a-chip by microcoil NMR, Lab Chip 5 (2005) 280–284.
[11] M. Kakuta, D.A. Jayawickrama, A.M. Wolters, A. Manz, J.V. Sweedler, Micromixer-based time-resolved NMR: applications to ubiquitin protein conformation, Anal. Chem. 75 (2003) 956–960.
[12] P.J.M. van Bentum, J.W.G. Janssen, A.P.M. Kentgens, J. Bart, J.G.E. Gardeniers, Stripline probes for nuclear magnetic resonance, J. Magn. Res. 189 (2007) 104–113.
[13] A.P.M. Kentgens, J. Bart, P.J.M. van Bentum, A. Brinkmann, E.R.H. van Eck, J.G.E. Gardeniers, J.W.G. Janssen, P. Knijn, S. Vasa, M.H.W. Verkuijlen, High-resolution liquid- and solid-state nuclear magnetic resonance of nanoliter sample volumes using microcoil detectors, J. Chem. Phys. 128 (2007) 1–17.
[14] J. Bart, A.J. Kolkman, A.J. Oosthoek-de Vries, K. Koch, P.J. Nieuwland, J.W.G. Janssen, P.J.M. van Bentum, K.A.M. Ampt, F.P.J.T. Rutjes, S.S. Wijmenga, J.G.E. Gardeniers, A.P.M. Kentgens, A microfluidic high-resolution NMR flow probe, J. Am. Chem. Soc. 131 (2009) 5014–5015.
[15] H.G. Krojanski, J. Lambert, Y. Gerikalan, D. Suter, R. Hergenroder, Microslot NMR probe for metabolomics studies, Anal. Chem. 80 (2008) 8668–8672.
[16] L.V. Blake, Transmission Lines and Waveguides, John Wiley & Sons, Inc., New York, 1969.
[17] C. Schöllhorn, W. Zhao, M. Morschbach, E. Kasper, Attenuation mechanisms of aluminum millimeter-wave coplanar waveguides on silicon, IEEE Trans. Electron Dev. 50(3) (2003) 740–746.
[18] J. Krupka, J. Breeze, A. Centeno, N. Alford, T. Claussen, L. Jensen, Measurements of permittivity, dielectric loss tangent, and resistivity of float-zone silicon at microwave frequencies, IEEE Trans. Microwave Theory Tech. 54(11) (2006) 3995–4001.
[19] R.-Y. Yang, C.-Y. Hung, Y.-K. Su, M.-H. Weng, H.-W. Wu, Loss characteristics of silicon substrate with different resistivities, Microwave Opt. Technol. Lett. 48 (9) (2006) 1773–1776.
[20] B. Rong, J.N. Burghartz, L.K. Nanver, B. Rejaei, M. van der Zwan, Surface-passivated high-resistivity silicon substrates for RFICs, IEEE Electron Dev. Lett. 25(4) (2004) 176–178.
[21] M. Spirito, F.M. De Paola, L.K. Nanver, E. Valletta, B. Rong, B. Rejaei, L.C.N. de Vreede, J.N. Burghartz, Surface-passivated high-resistivity silicon as a true microwave substrate, IEEE Trans. Microwave Theory Tech. 53(7) (2005) 2340–2347.
[22] J.T.M. van Beek, M.H.W.M. van Delden, A. van Dijken, P. van Eerd, A.B.M. Jansman, M.H.W. Kemmeren, T.G.S.M. Rijks, P.G. Steeneken, J. den Toonder, M.J.E. Ulenaers, A. den Dekker, P. Lok, N. Pulsford, F. van Straten, L. van Teeffelen, J. de Coster, R. Puers, High-Q integrated RF passives and RF-MEMS on silicon, Proceedings of the Mat. Res. Soc. Symp. 783 (2004).
[23] S. Chang, S. Sivoththaman, Low loss inductors built on PECVD intrinsic amorphous silicon for RF integrated circuits, in: Proceedings of the 18th Annual Canadian Conference on Electrical and Computer Engineering (CCECE05), Saskatoon, Canada, May 1–4, 2005.
[24] J.H. Klootwijk, H. van Kranenburg, C. Cobianu, V. Petrescu, P.H. Woerlee, H. Wallinga, An intensive study of LPCVD silicon morphology and texture for non-volatile memory application, in: Proceedings of the 25th European Solid State Device Research Conference, ESSDERC'95, 1995, pp. 383–386.
[25] http://femm.foster-miller.net/wiki/HomePage, David Meeker, dmeeker@ieee.org.
[26] http://www.cst.com, CST AG, Darmstadt, Germany.
[27] D.I. Hoult, R.E. Richards, The signal-to-noise ratio of the nuclear magnetic resonance experiment, J. Magn. Reson. 24 (1976) 71–85.

[28] F.D. Doty, G. Entzminger, Y.A. Yang, Magnetism in high-resolution NMR probe design. I: General methods, Concepts Magn. Res. 10 (3) (1998) 133–156.

[29] M.E. Lacey, R. Subramanian, D.L. Olson, A.G. Webb, J.V. Sweedler, High-resolution NMR spectroscopy of sample volumes from 1 nL to 10 μL, Chem. Rev. 99 (1999) 3133–3152.

[30] F. Laermer, A.R. Schlip, Method of anisotropically etching silicon, US Patent Nos. 4.855.017 and 4.784.720, 1991 and German Patent No. 4241045C1, 1990.

[31] M.J. Madou, Fundamentals of microfabrication, CRC Press, Boca Raton (FL), USA, 2002.

[32] F. Niklaus, G. Stemme, J.-.Q. Lu, R.J. Gutmann, Adhesive wafer bonding, J. Appl. Phys. 99 (2006) 031101–031128.

[33] J. Bart, R.M. Tiggelaar, M. Yang, S. Schlautmann, H. Zuilhof, J.G.E. Gardeniers, Room-temperature intermediate layer bonding for microfluidic devices, Lab Chip, unpublished results.

[34] J.D. van Beek, MatNMR: A flexible toolbox for processing, analyzing and visualizing magnetic resonance data in Matlab, J. Magn. Reson. 187 (2007) 19–26.